

## Chapter 7

# Diplexer and Triplexer Circuits

### 7.1 Introduction

In chapters 5 and 6, we presented data that suggest the sinuous antenna can couple to TES bolometers and provide a large boost in bandwidth over narrow-band antennas like the crossed double-slot. However, to control for foregrounds, we need to divide this bandwidth into narrow channels with microstrip circuits, which is the subject of this and the next chapter.

This chapter begins with a discussion of photometry vs spectroscopy to address why we chose simple channelizing circuits over an autocorrelator design that more directly mimics the FTS described in the last chapter. The simplest possible schemes are diplexer and triplexer circuits that extract two and three non-adjacent bands for observation in a terrestrial experiment. We discuss the design methodology of these circuits and show data from dual polarized antenna-coupled bolometers with desirable beam and spectral characteristics.

We have also fabricated a broadband Anti-reflection coating that uses three layers of monotonically increasing index. We discuss the design methodology behind this and show encouraging prototype test results.

## 7.2 Filter Manifolds vs Autocorrelation

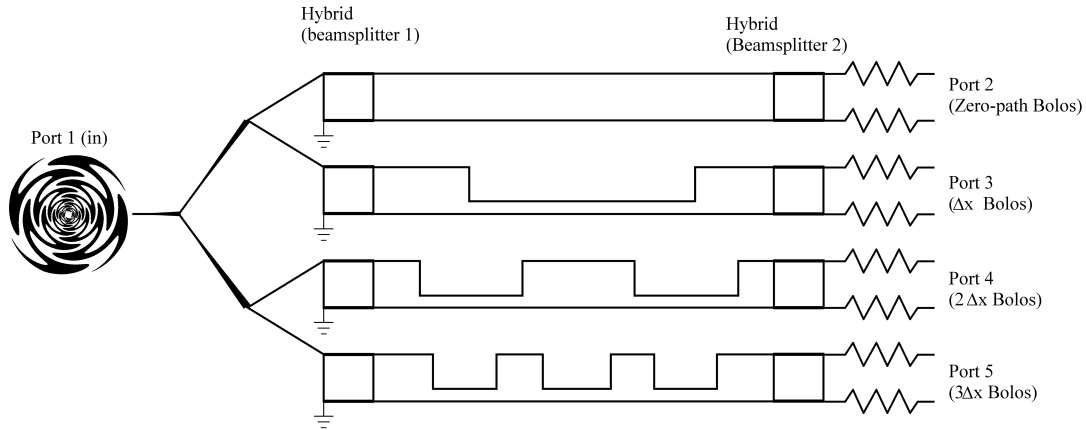


Figure 7.1. Schematic design of an autocorrelator in an antenna-coupled bolometer. In practice, we need several more bifurcations to Nyquist sample up to the lowest optical filter's cutoff.

This chapter and the next focus on microstrip filter manifold that sort the antenna's bandwidth into narrow frequency channels. However, in the previous chapter, we reported on successful spectral measurements of millimeter wavelength devices using a Fourier Transform Spectrometer. This motivates a natural question: Can we implement a similar autocorrelation spectrometer on our chips in microstrip circuits in lieu of filter manifolds?

For example, a cascade of microstrip-tees as shown in Figure 7.1 could split the broad-band output of each polarization of the sinuous into full-bandwidth lines with equal power. A set of quadrature hybrids playing the role of a beam splitter could then divide each line into two arms, one with a phase delay relative to the other. Finally, a second set of hybrids could re-combine the signals and terminate all the power of bolometers. In principle, this design could provide arbitrary resolution, limited only by the length of the longest arm. Additionally, we could low-pass filter the signal between the antenna and bifurcation so we would only need to bifurcate enough to Nyquist sample up to that cut-off. The primary challenges behind implementing this scheme are building a hybrid with two octaves bandwidth and keeping the loss in the lines between the hybrids low.

Even if these challenges are met, Zmuidzinas argued in a series of papers ((*Zmuidzinas*

[2003a]) and *Zmuidzinas* [2003b]) that this design is only tenable when the incident radiation has high occupation number ( $n(\nu) \gg 1$ ). We summarize those arguments here since they are an important part of our design decisions that eliminate on-chip autocorrelation as a possibility for CMB polarimetry detector designs.

The discrete Fourier transform of an interferogram does not perfectly re-construct the frequency spectrum. Instead, it results in a histogram where the spectrum is resolved into a basis of displaced top-hat functions:

$$n(\nu) = \sum_{c=1}^{N_{chan}} n_c \Pi_c(\nu) \quad (7.1)$$

where

$$\Pi_c(\nu) = \begin{cases} 1 & : \nu_c \leq \nu \leq \nu_{c+1} \\ 0 & : \text{else} \end{cases}$$

and  $n_c$  is the number of photons in a channel  $c$  between  $\nu_c$  and  $\nu_{c+1}$ . The length of the longest path determines the resolution  $\Delta\nu = \nu_{c+1} - \nu_c$  while the number of bifurcations determines the highest resolvable frequency  $\nu_{N_{chan}}$ . Expanding the incident spectrum in this basis, the energy received by the  $i^{th}$  bolometer (Equation 3.2) during time  $\tau$  is

$$\begin{aligned} E_i^{(B)} &\equiv \tau \langle d_i \rangle \\ &= \sum_c \{ (h\nu_c) \tau n_c \Delta\nu \} \left[ \frac{1}{\Delta\nu} \int_{\nu_c}^{\nu_{c+1}} d\nu |S_{i1}(\nu)|^2 \right] \equiv \sum_c E_c^{(f)} p_{ic} \end{aligned} \quad (7.2)$$

where the term in curled brackets is the energy  $E_c^{(f)}$  in one frequency channel and the term in square brackets is the probability  $p_{ic}$  that photons from frequency channel  $c$  are received by bolometer  $i$ .

Meanwhile, the energy covariance in the detectors (Equation 3.3) expanded in  $\Pi_c(\nu)$  is

$$\begin{aligned}
C_{ij}^{(B)}(\nu) &\equiv \tau^2 \sigma_{ij}^2 \\
&= h\nu E_i^{(B)} \delta_{ij} + \sum_c (h\nu_c) n_c \{ (h\nu_c) \tau n_c \Delta\nu \} p_{ic} p_{jc} \left[ \frac{1}{p_{ic} p_{jc} \Delta\nu} \int_{\nu_c}^{\nu_c+1} d\nu |S_{i1}(\nu)|^2 |S_{j1}(\nu)|^2 \right] \\
&\equiv h\nu E_i^{(B)} \delta_{ij} + \sum_c h\nu_c n_c E_c^{(f)} p_{ic} p_{jc} \rho_{ijc}
\end{aligned} \tag{7.3}$$

. The figure  $\rho_{ijc}$  (in square brackets of second line) expresses the probability that photons in channel  $c$  stimulate correlated responses in bolometers  $i$  and  $j$ . In the limit of high occupation number in the incident beam ( $n_c \gg 1$ ), the second term of the covariance is dominant. For an auto-correlation spectrometer,  $\rho_{ijc} \approx 1$ , so the covariance between bolometers is

$$C_{ij}^{(B)} = \sum_{c,c'} p_{ic} \left( \frac{(E_c^{(f)})^2}{\Delta\nu_c \tau} \delta_{cc'} \right) p_{c'j} \tag{7.4}$$

In an autocorrelation spectrometer, the vector of energies received by the bolometers  $E_i^{(B)}$  needs to be transformed into a vector of energies in each spectral channel through a Fourier transform, which in this case is the inverse probability matrix:  $E_c^{(f)} = \sum_i p_{ic}^{-1} E_i^{(B)}$  (*Bell* [1972]). The covariance of energy fluctuations in the bolometers transforms into a *diagonal* spectral covariance:

$$\begin{aligned}
C_{cc'}^{(f)} &\equiv \sum_{i,j} p_{ij}^{-1} C_{ij}^{(B)} p_{jc'}^{-1} \\
&= \frac{(E^{(f)})^2}{\Delta\nu_i \tau} \delta_{cc'}
\end{aligned} \tag{7.5}$$

So the fluctuations  $E^{(f)}/\sqrt{\Delta\nu\tau}$  are uncorrelated and independent of  $p_{ic}$ . Since the choice of  $p_{ic}$  is arbitrary, autocorrelation can provide sensitivities comparable to filter manifolds. Recall that a filter manifold has diagonal  $p_{ic}$  and the data does not need to be Fourier transformed.

However, in the low occupation number limit ( $n_c \ll 1$ ), the first term of  $C_{ij}^{(B)}$  dominates. While this matrix is diagonal, the Fourier transformed frequency correlations are not, which

can add considerably to the noise in each frequency channel. We can avoid this problem if  $p_{ic}$  is diagonal, in which case the frequency spectrum's covariance is also diagonal and independent of  $p_{ic}$ :

$$C_{cc'}^{(f)} = E_c^{(f)} \delta_{cc'} \quad (7.6)$$

and each channel has Poisson statistics. But as noted above, the probabilities  $p_{ic}$  are only diagonal when we use a filter bank to sort the frequency channels into separate bolometers.

In the low occupation limit ( $n_c \ll 1$ ), the signal-to-noise ratio of a measurement relative to a filter bank degrades as  $\sqrt{N_{chan}}$ , so it is very costly to use autocorrelation. To be specific, if the incident power is composed of 2.7K CMB photons and little additional loading (as in a satellite mission), the plank distribution exceeds  $n_c = 1$  above 40GHz. A spectrometer that achieves 2GHz resolution up to 300GHz has a sensitivity 12 times lower than a filter bank. Even from the ground where atmospheric loading produces an effective temperature of 30K,  $n_c$  only exceeds unity above 300GHz and the sensitivity is degraded by a factor of several. As a result of these considerations, filter banks are decidedly superior to autocorrelation for multi-chroic CMB detectors except for applications where high resolution spectroscopy is required. Current and future experiments all favor high mapping speeds over spectral resolution.

### 7.3 Terrestrial Measurements

The atmosphere absorbs and emits in the millimeter range as well, and this is a concern for any terrestrial experiment. However, the atmosphere does not absorb continuously; it is active only at specific spectral lines. Figure 7.1 shows the atmospheric transmission as simulated by the Caltech Submillimeter Observatory (CSO) for precipitable water vapor content at sites on White Mountain (Eastern California), the Atacama Desert (Chile), and the South Pole. The peaks at 60 and 120 GHz are from O<sub>2</sub> and are present with the same intensity at all locations. The line at 183GHz and the loading in the 200-300 GHz range

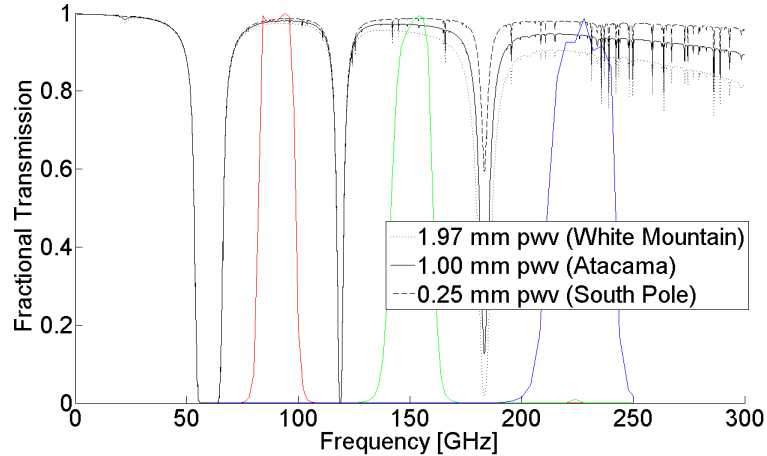


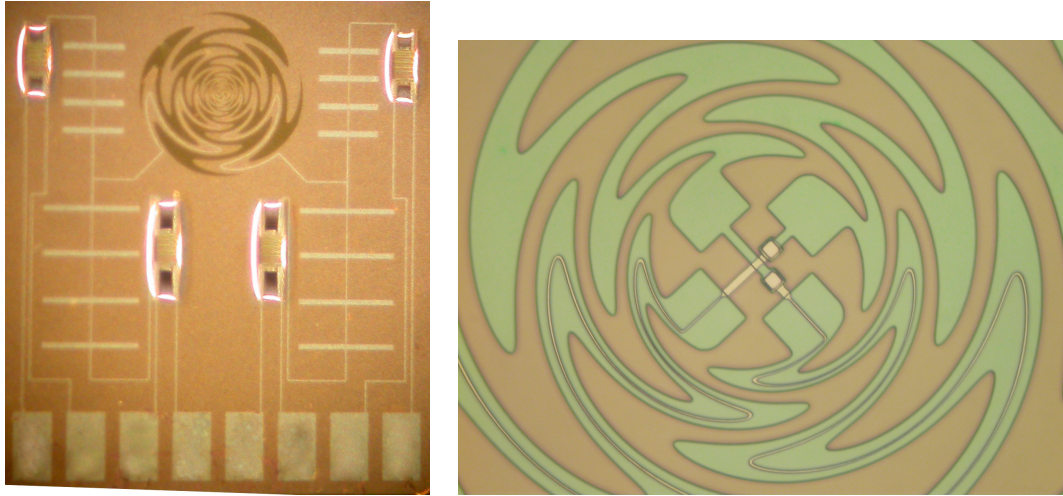
Figure 7.2. Atmospheric Transmission for typical Precipitable Water Vapors (PWV). We have co-plotted a simulation of our Triplexer circuit to illustrate where observing bands can be placed between lines. Atmospheric Data from (*Lis* [2010]).

are from  $H_2O$  and their strength depends on how dry the observing location is (*Pardo et al.* [2001]). These features are also not uniform across the sky (*Bussmann et al.* [2005]).

It is crucial that our detectors receive limited power from these lines, since they have an effective temperature of 30K. Not only will they overpower the extraterrestrial signals of interest, but their high power can also saturate our detectors and drive them normal. Several experiments have deployed with bands spaced in between these lines at 90GHz, 150GHz, and 220GHz. For example, SPT has a focal plane with these bands so they can look for Sunyaev-Zeldovich spectral distortions to identify high-redshift galaxy clusters. However, this experiment, like most others, only receives one of those three channels in each detector (*Carlstrom et al.* [2009]).

A notable exception to this design methodology is SuZie-II, which had four Winston-cone horns in its focal-plane that each fed three detectors behind the horns centered at three different bands. While the optical throughput was not uniform across all four channels, each pixel did simultaneously receive 150, 200, 350 GHz. The highest channel received significant loading from atmospheric water vapor and the researchers used this to monitor and control for atmospheric fluctuations (*Benson et al.* [2003]). The multi-chroic detectors described in this chapter could allow for similar control.

## 7.4 Diplexer Circuits



(a) 90GHz-150GHz Diplexers

(b) Feed in Antenna Center

Figure 7.3. Dual Polarized Sinuous Antennas coupled to TES-Bolometers through Diplexers (a). The Antenna is 1.2mm in diameter and the interior feed (b) drives the  $H$ - $V$  Excitation

The simplest filter-bank design branches two filters with non-contiguous pass-bands from a common node (See Figure 7.3). Each filter has an impedance that matches that of the input and output transmission lines' ( $10\Omega$ ) at resonance, but is reactive off resonance. While this is necessary to reject out-of-band power, it also complicates the multi-channel circuit's design. Looking from the antenna side into microstrip-T, the out-of-band filter will present a complex impedance in parallel to the in-band filter's  $10\Omega$  that can reflect away much of the incident power.

As discussed in the Chapter 6, a transmission line transforms the impedance of a load to an input impedance that is a function of the length and impedance of the transforming line (see Equation 6.9). We chose the length and impedance of each line between the node and filter such that at the filter's band-center, the input impedance from the other filter is infinite (open). Figure 7.4 illustrates this. The impedance of a filter changes rapidly at the band edge, so the bands in this circuit cannot be adjacent. Fortunately, the atmospheric lines require non-contiguous bands, so this design methodology is still appropriate for focal planes

in terrestrial experiments. In Chapter 8, we discuss a design that allows for contiguous bands that would be desirable for a balloon-born or satellite mission.

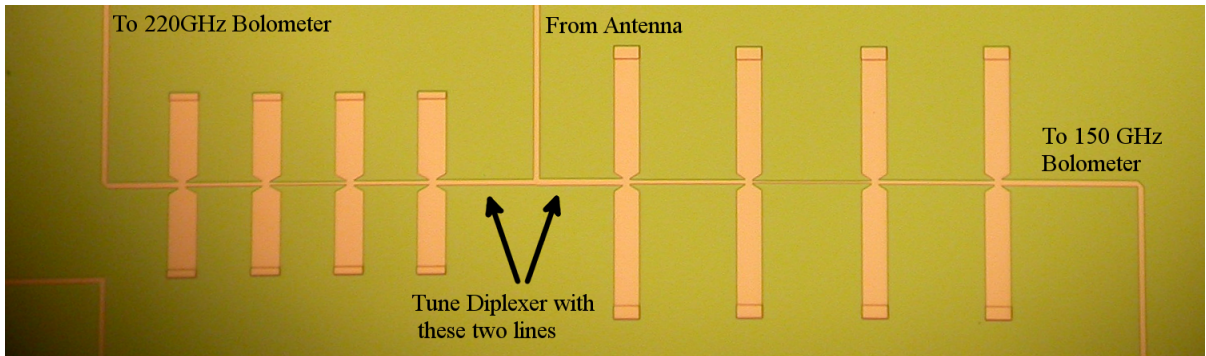


Figure 7.4. 150-220GHz Diplexer

#### 7.4.1 Prototype pixel design

Figure 7.3(b) shows the interior of the sinuous antenna and reveals that it is fed in the  $(H - V)$  modes. This feed only uses one microstrip per polarization and significantly simplifies the wiring between the antenna and filter-bands. Additionally, the required  $180^\circ$  phase is established by the microstrip antenna feed and we no longer need a differentially fed load in the bolometer interior. The thermalizing load near the TES is a coiled stretch of transmission line that gradually transitions from superconducting Nb to lossy Al-Ti. This is visible in Figure 3.5 Finally, *both* polarizations are wired to bolometers through filter banks in these devices.

Spectral measurements from Chapter 6 suggest that the wave speed in our transmission lines is lower than expected, so we compensated by shortening the length of all the stubs and inverters in our filters by 10% (based on recent measurements from another project *Arnold* [2008]). Finally, we used 4-pole filters instead of 3-pole because we require the steep roll-off to suppress interactions between the channels in frequency-space.

### 7.4.2 Diplexer Spectroscopy

We subjected these devices to the same battery of optical tests described in chapter 6 with the same optical test cryostat. However, these detectors (and the ones from Chapter 8) saturate while exposed to 300K radiation through the filter stack described in chapter 6. To avoid saturating the detectors, we shaded them with 0.635cm (0.25”) of MF110 stycast. In all figures of optical throughput, we divided away the additional loss associated with the stycast attenuator since this loss is ultimately necessitated by the bolometer’s non-ideal thermal characteristics and is not a property of the microwave circuits we are actually trying to test. We characterized the loss from the stycast by repeating a set of measurements with twice the stycast 1.27cm (0.5”). The loss associated with 0.25” stycast is just the ratio of the two measurements and we summarize these loss parameters in Table 7.1.

Table 7.1. Optical Power Transmission through MF110

| $f_{center}$ | Fractional Transmission |
|--------------|-------------------------|
| 90           | 55%                     |
| 150          | 29%                     |
| 220          | 11%                     |

We also used 14mm diameter sintered-alumina lenses instead of Silicon because they are cheaper and more mechanically durable. The relative permittivity is 10.5 and the loss tangent of Alumina at 300K is  $\tan(\delta) \sim 1 - 10 \times 10^{-4}$ , so it is an acceptable substitute for the more brittle silicon. As in chapter 6, we coated each lens with a single layer of ultem-1000. For the 90-150GHz diplexer, we used a 0.35mm (0.014”) thick film (nominally centered at 120GHz), while for the 150-220GHz diplexer, we used an 0.23mm (0.009”) thick film (nominally centered at 180GHz). The alumina extension was 2.43mm thick, so the optical path length through this material *plus* that through the 0.5mm silicon substrate produces the correct phase delay to form a synthesized ellipse.

Figure 7.5 shows the spectral response of the detectors in both polarizations of both the diplexers. The pass-bands are only 3% low, and have 15% fractional bandwidths that match their designs. We made the bands conservatively narrow to avoid atmospheric lines; with better control over pass-band center, we should be able to safely expand the filter

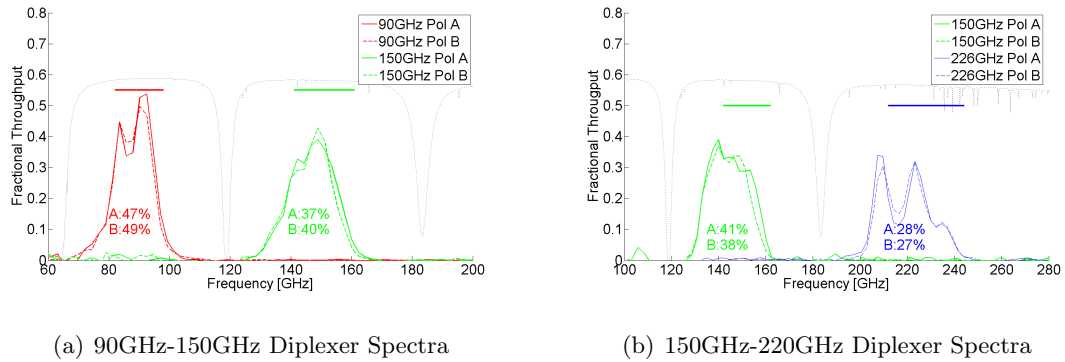


Figure 7.5. Measured Spectra for the Diplexer circuits. The vertical axis is total receiver throughput. The black dashed line shows the atmosphere in arbitrary units and the horizontal lines show the designed -3dB bandwidth. We list the band-averaged throughputs for each channel as well.

bandwidths in future designs. Some of the bands exhibit fringing that is reminiscent of the fringing in the single filter prototypes (chapter 6), but there is no obvious mismatch at the bolometer’s distributed load. We have not been able to trace the fringes to specific lengths due to the complexity of this circuit.

The optical throughputs are slightly lower than comparably located bands in the devices from chapter 6. One possible explanation is that our microstrip feed depicted in Figure 7.3(b) is not driving the antenna in a purely odd mode, but rather in a superposition of the even and odd mode. Since the even mode has a quadrupolar pattern that vanishes on boresight, a partial excitation of this mode might slightly degrade the throughput. Alternatively, the alumina lens material may be more lossy than expected. Owing to instability of our spectrometer’s lamp, we have not yet managed to measure the loss in our lens material.

## 7.5 Triplexers with broad-band anti-reflection coated lens

The Diplexer circuit design can easily generalize to three bands in a circuit called a Triplexer shown in Figure 7.6. This circuit has three bands centered at 90, 150, and 226GHz. Because each line between the branching node and filter has two free parameters - the length and impedance - they can transform their filters’ impedance into an open in the center of

the two other filters' pass-bands. The simulated scattering parameters of this circuit are shown in Figure 7.2.

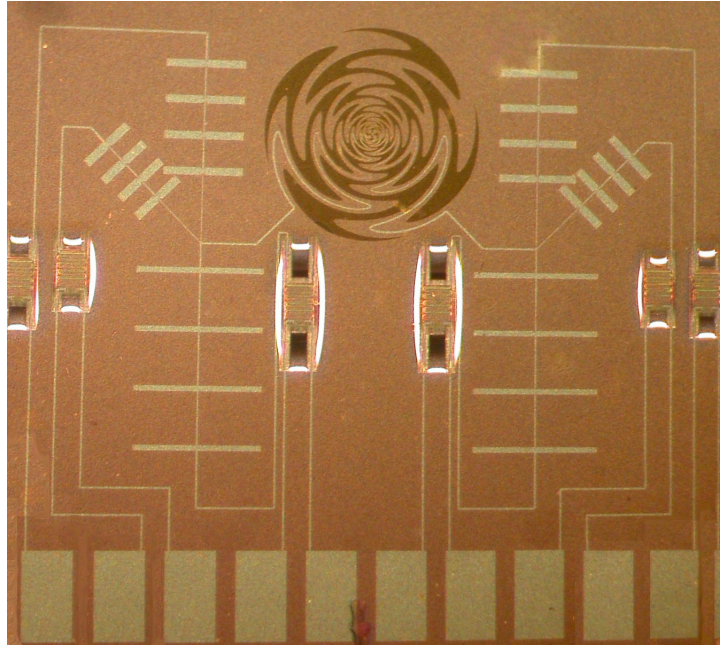


Figure 7.6. Sinuous Antenna coupled to TES bolometers through two Triplexers.

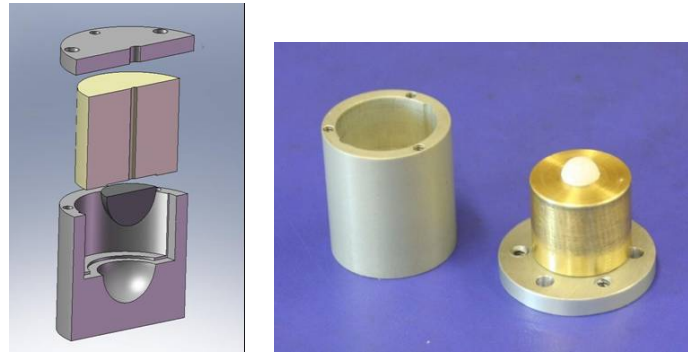
The single anti-reflection coating does not have a sufficient bandwidth to cover all three channels, so we implemented a multilayer coating instead. The coating has two layers of TMM from the Roger's corporation and one of porous Teflon. TMM is a circuit board material whose index can be adjusted by loading with a proprietary high-dielectric dopant. Roger's Corp sells TMM as preset boards with relative permittivities of 3, 4, 6, and 10. While Roger's Corp's intended application of these boards is for microwave frequency circuits, we have measured the loss-tangents and relative permittivities in the millimeter spectral range with a Fourier Transform Spectrometer and concluded that they still have the same designed permittivities and have acceptably low loss tangents of  $\tan(\delta) \sim 10^{-3}$ .

Roger's Corp forms their circuit boards by thermosetting the material in a mold. We have specially obtained *un*-thermoset TMM from Rogers so we can mold it onto the hemispherical contacting lenses. We machined a series of presses shown in Figure 7.7 that apply films summarized in Table 7.2. The surfaces of the press must be anodized to keep the

coatings clean of aluminum-oxide residue. We set each film in the press in a N<sub>2</sub> oven at 300 °C for 1 hour and encourage adhesion between layers with a thin layer of Stycast 1266 that we apply after baking. The outer-most layer is porous Teflon (porex) that we thermoset at a much lower temperature of 90 °C. The design thicknesses and permittivities are summarized in Table 7.2

Table 7.2. 3-layer Antireflection Coating Designed Parameters

| Material      | nominal $\epsilon_r$ | thickness [inches] |
|---------------|----------------------|--------------------|
| Alumina       | 10.5                 | NA                 |
| TMM6          | 6                    | 0.007              |
| TMM3          | 3                    | 0.010              |
| Porous Teflon | 1.4                  | 0.015              |
| Vacuum        | 1                    | NA                 |



(a) Mechanical Drawing of AR-coating press (b) Photograph of Press with lens

Figure 7.7. 3-layer Anti-reflection coating press

Table 7.3. Throughput with and without the 3-layer coating

| Channel   | Throughput, no coating | Throughput with coating | Fractional increase |
|-----------|------------------------|-------------------------|---------------------|
| 90 GHz A  | 34%                    | 44%                     | 29%                 |
| 90 GHz B  | 35%                    | 44%                     | 27%                 |
| 150 GHz A | 26%                    | 33%                     | 28%                 |
| 220 GHz A | 22%                    | 26%                     | 19%                 |
| 220 GHz B | 21%                    | 24%                     | 17%                 |

We characterized the detectors' spectra as with the diplexer circuits and show those results in Figure 7.8. Because of a design flaw, one of the two 150GHz channels was open

between the filter and bolometer and provided no useful data. As table 7.3 indicates, the coating enhanced the throughput by nearly 30%.

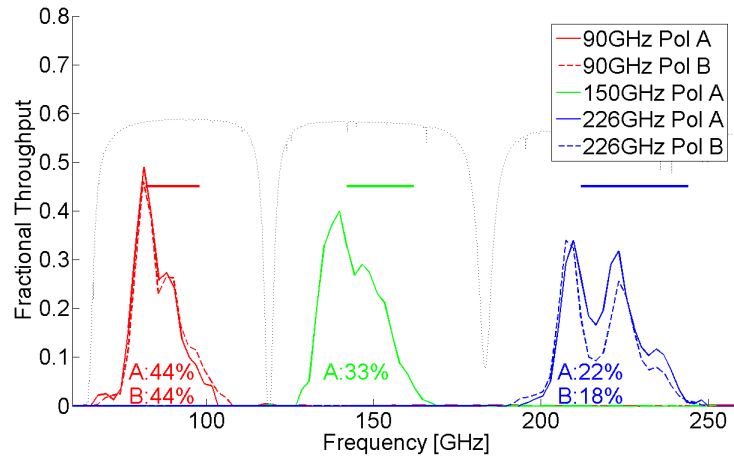
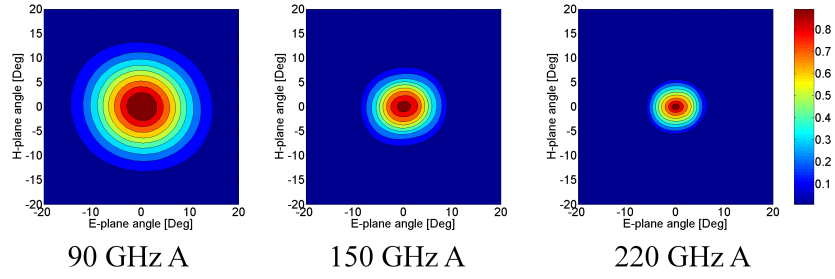


Figure 7.8. Triplexer Spectra. Vertical axis is total receiver throughput. The dashed line is 1mm pwv atmosphere, arbitrary units. Band Averaged throughputs are listed under spectra. 150B yielded no useful data because of a design flaw.

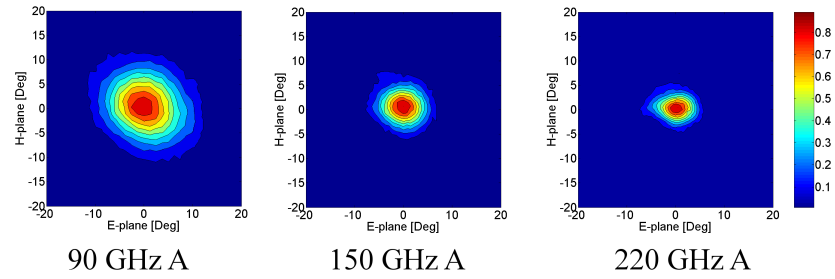
## 7.6 Beams of single-ended feed Sinuous

The simplified feeding scheme shown in Figure 7.3(b) is significantly different from that used in Chapter 6 (Figure 8.11(b)). As noted above, this may be responsible for the slightly decreased efficiencies in the diplexer and triplexer devices compared to the devices from chapter 6, but further measurements are needed to confirm this. However, the feed seems to impact the beam ellipticity in a more significant way. We measured the beam shapes with the chopped thermal load, similar to the measurements in Chapter 6. The same bands in the diplexer and triplexer circuits had very similar beams, so we only show the triplexer beams in Figure 7.9 for brevity.

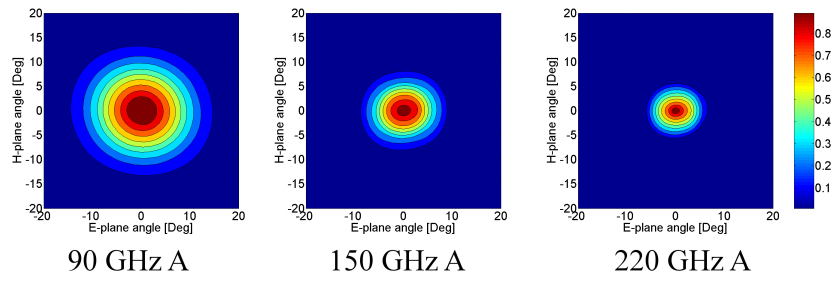
We note that the beams in the 220GHz channels are elliptical (see Table 7.4). Simulations of just the antenna (without the lens) show that the feed slightly steers the beam off boresight by roughly  $2^\circ$  compared to the balanced feed in Chapter 6. Diffraction of this steered beam through the lens then generates a ellipticity comparable to and in the same



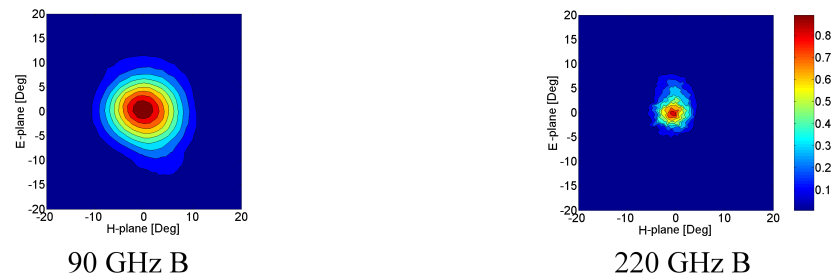
(a) 2-D Beam Simulations, Pol A



(b) 2-D Beam Measurements, Pol A



(c) 2-D Beam Simulations, Pol B



(d) 2-D Beam Measurements, Pol B

Figure 7.9. Simulations and Measurements of Triplexer device beams.

direction as the measurements. Several experiments deploying over the next years will help demonstrate what levels of beam ellipticity are tolerable. Theoretical studies suggest that a telescope with beams exceeding 4% ellipticity will not be able to detect primordial B-modes with  $r < 0.1$  without some optics to control or suppress this systematic.

Table 7.4. Beam Geometry

| Channel   | ellipticity       | E-plane FWHM               | H-plane FWHM               | Boresight Cross-Pol Rejection |
|-----------|-------------------|----------------------------|----------------------------|-------------------------------|
| 90 GHz A  | $5.4\% \pm 0.3\%$ | $11.1^\circ \pm 0.5^\circ$ | $10.8^\circ \pm 0.5^\circ$ | $2.7\% \pm 1.7\%$             |
| 90 GHz B  | $4.6\% \pm 0.3\%$ | $11.3^\circ \pm 0.5^\circ$ | $10.7^\circ \pm 0.5^\circ$ | $2.3\% \pm 0.7\%$             |
| 150 GHz A | $1.1\% \pm 0.1\%$ | $7.0^\circ \pm 0.2^\circ$  | $6.2^\circ \pm 0.2^\circ$  | $3.4\% \pm 2.7\%$             |
| 220 GHz A | $9.6\% \pm 0.5\%$ | $6.0^\circ \pm 0.5^\circ$  | $4.9^\circ \pm 0.5^\circ$  | $4.9\% \pm 3.4\%$             |
| 220 GHz B | $7.7\% \pm 1.8\%$ | $5.6^\circ \pm 0.8^\circ$  | $4.4^\circ \pm 0.8^\circ$  | $5.1\% \pm 4.6\%$             |

We can mitigate this effect by rotating a cryogenic broad-band half-waveplate or by using a sufficiently large primary such that these features are a smaller scale on the sky than any relevant CMB temperature anisotropies. Researchers have developed half-waveplates with more than an octave bandwidth and upcoming experiments may demonstrate that we need waveplates even with perfectly circular beams *Pisano et al.* [2006]. However, we would like to avoid these strategies for high-altitude measurements where weight and moving cryogenic components can greatly increase an experiment's cost.

Differentially feeding lumped rf-loads at the bolometers avoids this problem in the narrow-band devices, but it is not practical to extend this scheme to multi-channel pixels. Multi-channels pixels with differentially fed loads would require much longer lengths of transmission line that would greatly increase dielectric losses. Additionally, those circuits would need uniform films and etch properties across a surface area of several square millimeters to avoid the phasing errors that those circuits would be trying to avoid in the first place. The Polarbear detectors described in chapter 4 manage to avoid this by maintaining a small footprint, but the multichroic pixels would have a footprint similar to the lens. The Caltech/JPL phased antenna arrays show beam asymmetries that the team traces to non-uniform films, and those have a similar footprint to our multichroic pixels. We describe a possible feeding circuit in the concluding chapter (chapter 9) that may solve this problem.

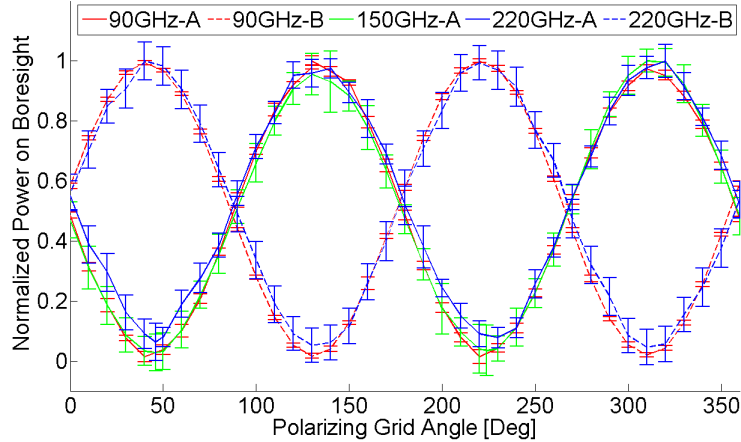


Figure 7.10. Optical response to the chopped load on boresight through a polarizing grid. Again, 150B yielded no useful data because of a design flaw.

The antenna rejects cross-polarized power to 1.5% in the 90 and 150GHz (Figure 7.10), which is similar to the rejection in the devices of Chapter 6. The 220GHz channel leaks nearly 3% and this elevated leakage seems to come from the slight beam steering in the highest channel. As before, the leakage is far worse without the anti-reflection coating, leaking between 5 and 10%.

Finally, beam measurements suggest that the coating layers must be concentric with tight tolerances of roughly 1-mil centering. After damaging the press, we molded coatings onto a lens that had 2-3mil errors in alignment and we generated beams with high-asymmetry and strong coma-lobes. 1-mil tolerancing is possible, but must be strictly observed.

## 7.7 Conclusions

In this chapter we have demonstrated that we can couple a dual polarized sinuous antenna to diplexer and triplexer circuits that partition the bandwidth into narrow channels between atmospheric emission lines. The anti-reflection coating technology is also promising.

The specific designs show here cannot be easily extended to more than three channels because the lowest frequency filter's satellite band interacts with the higher frequency channels. However, other researchers have built four-channels filter banks by using quasi-lumped filters that do not have a satellite band. But even with this modification, the filter manifolds cannot support contiguous bands because the reactance of each filter would change too rapidly in the pass-band of their neighbor, making it impossible to tune away the impedance with a simple transmission line.

We solve this problem of non-contiguous bands in the next chapter with a log-periodic channelizer that intentionally exploits the off-resonance reactance of each filter instead of trying to tune it away. With this change, we can build filters with an arbitrary number of channels and contiguous bands.